Water Resources Research

RESEARCH ARTICLE
10.1029/2018WR023975

Algorithmic Characterization of Lake Stratification and Deep Chlorophyll Layers From Depth Profiling Water Quality Data

Wenzhao Xu[1], **Paris D. Collingsworth**[2], **and Barbara Minsker**[3]

[1]Department of Civil and Environmental Engineering, University of Illinois at Urbana–Champaign, Urbana, IL, USA, [2]Department of Forestry and Natural Resources and Illinois-Indiana Sea Grant, Purdue University, West lafayette, ID, USA, [3]Department of Civil and Environmental Engineering, Southern Methodist University, Dallas, TX, USA

Abstract We develop and test algorithms for rapidly and consistently analyzing water quality profile data such as temperature and fluorescence that are used to identify lake thermostratification and deep chlorophyll layers (DCL). Currently, the processing of profile data and identification of key features are manual and subjective, and thus, the results are not comparable from one sampling event to another. In this study, we develop a method to approximate vertical temperature profiles with linear segments using a piecewise linear representation algorithm, from which stratification patterns can be extracted. We also propose an automated peak detection algorithm to identify the location and magnitude of DCL. The algorithms are applied to water quality profile data collected by the United States Environmental Protection Agency Great Lakes National Program Office, which conducts annual depth profiling using conductivity, temperature, depth profilers at fixed locations in the Great Lakes. The algorithms generate similar results to human judgments, with some outliers that show expert errors, algorithm limitations, and ambiguities in defining layers. We also show how the algorithms can analyze the shape of temperature and fluorescence profiles to detect unusual patterns. Lake Superior is used as a case study to reveal spatial and temporal trends of the thermocline, DCL, and the heat storage change from spring to summer. The results reveal that more heat was stored in the eastern basin of the lake. The methods proposed here will help take full advantage of historical depth profiling data and benefit future sampling processes by providing a consistent method.

Key Points:
- Algorithms are developed for automatically identifying lake stratifications and DCL from conductivity-temperature-depth profiling data
- Algorithms perform similar to humans and reveal spatial and temporal patterns of lake stratifications and DCL in the Great Lakes
- Open-source Python code is provided

Supporting Information:
- Supporting Information S1

Correspondence to:
W. Xu,
xuwz.uiuc@gmail.com

Citation:
Xu, W., Collingsworth, P. D., & Minsker, B. (2019). Algorithmic characterization of lake stratification and deep chlorophyll layers from depth profiling water quality data. *Water Resources Research*, *55*, 3815–3834. https://doi.org/10.1029/2018WR023975

Received 29 AUG 2018
Accepted 6 APR 2019
Accepted article online 26 APR 2019
Published online 6 MAY 2019

1. Introduction

CTD (conductivity, temperature, depth) profilers are widely used to monitor the vertical distribution of water quality parameters in lakes and oceans. Effectively and efficiently analyzing and utilizing the information collected by these instruments is important because depth profiling data provide insights on key lake features such as lake thermostratification and deep chlorophyll layers (DCL). This study develops new methods and software for automating the detection of thermal stratification and DCL, thus improving reproducibility and speed of depth profiling data.

Thermal stratification of lakes occurs during the summer as the lighter and warmer surface water floats on the surface, forming a shallow epilimnion layer, while cooler, more dense water sinks to the bottom, forming the deep hypolimnion layer. The transition zone between the epilimnion and hypolimnion is the metalimnion, and the horizontal plane within the metalimnion that has the sharpest temperature gradient is called the thermocline (TRM). Wind speed is the most important factor that influences the depth of the TRM (Boehrer & Schultze, 2008), with larger wind stress generated by strong wind leading to a deeper TRM and more mechanical energy used to mix the lake.

In addition, the TRM depth can be tilted by internal seiche events (warmer surface water is pushed downwind while the cooler water below the TRM flows upwind), a process that may be affected by the Earth's rotation (Gorham & Boyce, 1989). For example, baroclinic motion generated a TRM depth oscillation with a period of 17 hr in Lake Erie (Bouffard et al., 2013). On the other hand, surface temperature, which is influenced by solar radiation, cloud cover, wind-driven mixing, water clarity, ice cover, and lake bathymetry (Moukomla & Blanken, 2016), exerts a strong influence on the stability of stratification patterns. High surface water temperature in the epilimnion often produces a very stable vertical water column stratification that requires large amounts of mechanical energy to modify or mix the layers (Austin & Colman, 2007;

Gorham & Boyce, 1989). The energy or radiation that a water body absorbs can be reduced by ice cover, leading to a later onset of stratification (Austin & Colman, 2007).

Deep chlorophyll layers (DCL), deep chlorophyll maximum (DCM; Camacho, 2006; White & Matsumoto, 2012), and subsurface chlorophyll maximum (SCM; Gong et al., 2015) are water layers with high chlorophyll concentrations that lie below the TRM in stratified lakes or oceans. In the Great Lakes, DCL is observed during the summer-stratification period and dissipates in late August when the TRM deepens and the metalimnion becomes unstable (Watkins et al., 2015). A significant portion of lake-wide primary production is found in the DCL, where the highest chlorophyll concentrations exist. For example, in the Great Lakes, studies have shown that chlorophyll concentrations in the DCL are 1.5 to 2.5 times higher than those in the epilimnion in Lake Superior (Barbiero & Tuchman, 2004) from 1996 to 2001 and 1.8 to 5.7 times higher in Lake Michigan from 1982 to 1984 (Fahnenstiel & Scavia, 1987). In Lake Michigan, DCL is responsible for 30% to 60% of areal primary production in Lake Michigan (Watkins et al., 2015). Furthermore, the phytoplankton community in the DCL is different from that in the epilimnion (Barbiero & Tuchman, 2004; Bramburger & Reavie, 2016). The DCL also affects energy and material transfer as it shifts the location and extent of food sources for grazers (Gong et al., 2015). The DCL formation and maintenance are mainly controlled by the light levels and nutrients, because algae need to find the best location to compete for these two resources (Klausmeier & Litchman, 2001). Other influencing factors on DCL formation include the following: (a) lake stratification timing, surface water temperatures (Barbiero & Tuchman, 2004), and internal wave motions (Bouffard et al., 2018); (b) stability in the upper mixed water layers (Ryabov et al., 2010); (c) phytoplankton mobility (Cullen, 2015) and phytoplankton photoacclimation or photoadaptation (phytoplankton increases the chlorophyll level when in a deficit of light; Barbiero & Tuchman, 2004; White & Matsumoto, 2012; Watkins et al., 2015; Scofield et al., 2017); (d) zooplankton grazing (Watkins et al., 2015) and zooplankton excretion (Oliver et al., 2014).

The USEPA-GLNPO (U.S. Environmental Protection Agency Great Lakes National Program Office) deploys Sea-Bird CTD profilers to monitor the Great Lakes every year. During sampling activities operators manually view downcast profiling (i.e., CTD data sampled as the profiler descends to the lake bottom) to identify the depths of the TRM, the boundaries among the epilimnion, metalimnion, and hypolimnion, and DCL. After these layers are identified, bottle samples are taken at these depths during upcast profiling (i.e., as the CTD profiler ascends to the lake surface). However, manual identification of these features has the following drawbacks: (1) mistakes can be made in manually identifying the layers, causing bottle samples to be misaligned with the desired depth; (2) each operator applies subjective criteria so that the depth recorded is not standardized and may not be comparable across operators; and (3) as more and more data are recorded, it becomes more and more difficult to check the historical records to find mislabeled or missing judgments. Although researchers can manually relabel the depths of all profiles after collection, this is a time-consuming process and the subjective criteria are still problematic. Thus, historically sampled data may remain buried in databases and not adequately utilized to guide future sampling activities.

Automated feature identification provides a potential solution to the challenges posed by CTD profiling data. To automatically identify lake stratification patterns, the simplest approach is called the isotherm approach, where TRM depth is defined with a preset temperature, which can either be a fixed temperature or dependent on locations (Wang et al., 2000) or profiles (Fiedler, 2010). Previous research has also identified TRMs using temperature gradients such as thermocline strength index (TSI; Yu et al., 2010) or indices based on density gradients such as Relative Thermal Resistance to Mixing (RTRM; Hampton et al., 2014), where the depth with maximum temperature gradient or maximum RTRM indicates the TRM location, respectively. Such methods are adequate for bottle-sampled data that are accurate and without much noise. However, with high-frequency sampled sensor data, the depth interval can be quite small and sampling noise or local fluctuations can lead to significant gradients that can bias the TRM location. Smoothing and aggregating data can reduce the effects of noise but may introduce errors from the choice of smoothing extent. Furthermore, these methods can only capture the location of the TRM and are not able to characterize other stratification features such as the locations of the epilimnion and hypolimnion.

Another approach for identifying stratification features is to approximate the temperature profiles using piecewise linear segments. This algorithm, called piecewise linear representation (PLR), has three approaches (Keogh et al., 2004): (a) bottom-up (merging small segments to generate a larger segment), (b) top-down

(partitioning large segments into smaller segments), and (c) sliding windows (building segments by adding points until approximation errors are too large). Thomson and Fine (2003) used split and merge algorithms based on the algorithm developed by Pavlidis and Horowitz (1974), which combines top-down and bottom-up approaches, to approximate density CTD profiles and identify mixed layers in ocean CTD profiles. Fiedler (2010) compared this algorithm with other TRM detection algorithms, mentioned above, in oceans. Yet the PLR method has not been extended to detect all features of lake stratifications (i.e., epilimnion, metalimnion, and hypolimnion).

For DCL identification, merely setting the maximum values as the location of the DCL is not reasonable when the fluorescence profile does not have a peak or multiple peaks exist such as with a bimodal distribution (Lips & Lips, 2014; Mellard et al., 2011). Researchers have previously approximated chlorophyll depth profiles using Gaussian distributions (Abbott et al., 1984; Gong et al., 2015; Richardson et al., 2002). The Gaussian model assumes that DCL shapes are symmetrical and have a constant chlorophyll concentration above and below the DCL, referred to as the background concentration. Uitz et al. (2006) slightly modified the Gaussian bell shape model by incorporating a linear term so that the background concentration can change below the DCL. However, in some systems such as the Great Lakes, a fluorescence profile may have an asymmetrical shape; therefore, the Gaussian shape assumption may not always be applicable for characterizing DCL.

In this study, we extend the PLR characterization method to not only detect the location of the TRM but also study the shapes of temperature profiles to identify epilimnion and hypolimnion and other patterns such as double TRMs in a robust way. To analyze the fluorescence profiles and identify the characteristics of the DCL, including location, thickness, and intensity of chlorophyll concentration (Beckmann & Hense, 2007; Gong et al., 2015), we first develop a peak detection algorithm based on the gradients of fluorescence concentrations. Then we fit the peak with two half-Gaussian shapes, which provides more flexibility than fitting a single shape and helps to overcome the asymmetry of the peak shape. These methods are described in section 2. We then apply the algorithms on data from the Great Lakes and validate them against operators' historical notes in section 3. We then demonstrate the usefulness of the algorithms through a case study of the spatiotemporal trends of lake stratifications, DCL, and heat storage change in Lake Superior. Section 4 discusses the implications of the results, followed by conclusions in section 5.

2. Methodology

The algorithm workflow is shown in Figure 1. Data preprocessing is first conducted to remove inaccurate data, aggregate data (i.e., standardize sampling depth intervals), and smooth fluctuations by computing moving averages. Then the algorithms detect lake stratification features using piecewise linear segmentation algorithms. Finally, the DCL is identified by detecting peaks of fluorescence concentrations. In the following sections, TRM, LEP, and UHY are used to represent the thermocline, lower epilimnion, and upper hypolimnion, respectively. (see Table 1).

2.1. Data Sources and Preprocessing

A Sea-Bird® CTD profiler measures water quality variables as it travels through the water. USEPA-GLNPO deploy the Sea-Bird CTD vertically to generate depth profiles at fixed geolocations in each lake (Figure 2) twice per year. The CTD is deployed with a specific upward and downward speed(s) to ensure consistency. The raw sampling time interval is usually 0.042 s. The sensors mounted are listed in Appendix A. During CTD deployments, the operators determine the TRM, epilimnion, hypolimnion, and DCL by visually assessing the raw data. The data analyzed in this study were collected from 1996 to 2013, with 1,665 profiles in total. The very raw sensor data are parsed into human readable files by the CTD's software. Each depth profile contains data on temperature, dissolved oxygen, beam attenuation coefficients, specific conductivity, pH, and fluorescence. Fluorescence is widely used as a proxy for chlorophyll concentration (Lorenzen, 1966), and the peak of fluorescence concentrations is assumed to be the location of the DCL. We use the downcast of the depth profiles for detection, as the operators do, because the data measured during the upcast are already disturbed by the downcast movement of the CTD profiler.

The following preprocessing steps are performed to remove noise, which can have significant effects on the results of PLR algorithm (Keogh et al., 2004):

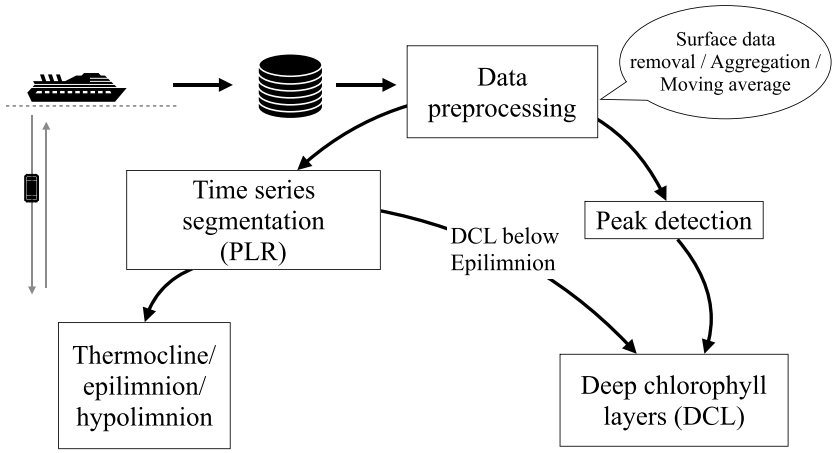

Figure 1. Algorithm workflow to detect lake stratification and deep chlorophyll layers. PLR = piecewise linear representation.

Step 1: Remove the lake surface data collected at depths less than 3 m. These surface data usually have anomalous spikes.

Step 2: Bin data with a 0.25-m interval (half of current USEPA-GLNPO protocols) and average the data in each bin.

Step 3: Smooth the data using a moving average filter with Hann window (Oppenheim et al., 1999), and window size of 2 m. The size of this smoothing window is chosen by trial and error to avoid excessive distortion in the profile data.

For step 3, a simple moving average approach is selected because it performed better than other smoothing algorithms, such as Fourier transformation or wavelet transformation, on the profile data. Fourier transformation requires a threshold to remove low energy frequencies, but the threshold cannot be easily identified as it has no clear physical meaning for limnological data. For the wavelet algorithm, the tuning parameter is the decomposition level, with only a few alternative values from which to choose. However, according to our tests, the wavelet smoothing algorithm can significantly change the depth of the maximum peak, so the peak detected after smoothing may not be the depth with the highest fluorescence in the raw data. Therefore, we chose the simplest approach of the moving average smoothing algorithm.

2.2. Lake Stratification Detection

The piecewise linear representation (PLR) approach approximates the profiling data using several linear segments. As mentioned in the introduction, we implement a bottom-up approach for identifying the appropriate linear segment size. In previous work, this approach has performed better than the top-down approach for various datasets (Keogh et al., 2004). The algorithm workflow is described in Figure 3 and the core steps are:

Step 1 *Initial segments*. Create initial segments to approximate profiling data by connecting two consecutive points. Therefore, Points 1 and 2 (starting from the lake surface) form the first segment (Seg_1), Points 3 and 4 form the second segment Seg_2, etc.

Step 2 *Compute errors for potential merge locations*. Calculate the approximation errors (E) of one segment (Seg_i) combined with the next segment (Seg_{i+1}). The errors represent how closely the linear segment approximates the data when Seg_i and Seg_{i+1} are combined.

Step 3 *Select merge locations*. Find the combination of segment i,i+1 that generates the smallest error. If this smallest error is less than the error threshold, E_{max}, go to Step 4. Otherwise, stop and output the segments that remain.

Step 4 *Merge*. Combine the segment i,i+1, go to Step 2.

Table 1
Acronyms

Acronyms	Definition
TRM	Thermocline
DCL	Deep chlorophyll layers
UHY	Upper hypolimnion (boundary between metalimnion and hypolimnion)
LEP	Lower epilimnion (boundary between epilimnion and metalimnion)

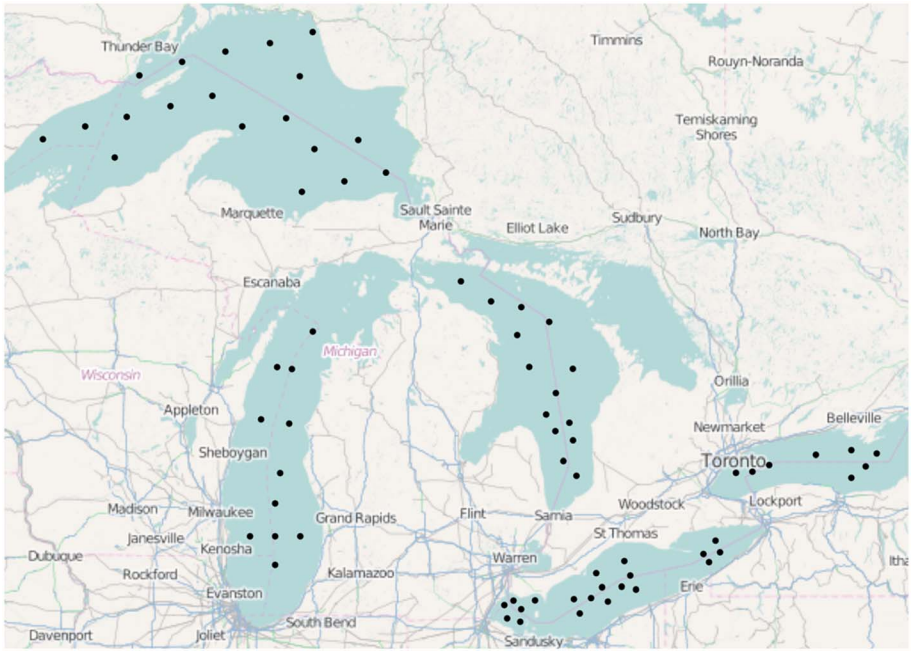

Figure 2. SeaBird^{TM} Conductivity, temperature, depth sampling locations in the Great Lakes.

In our implementation, the linear segments that approximate the raw data are produced by linear regression using the least squares method. The approximation error E is determined by the maximum discrepancies of the linear segment approximation and the raw series. Through trial and error, by manually comparing the detected layers with operators' notes, we select $E_{max} = 0.3^{\circ}$C, indicating that the linear segment approximation will have at most 0.3 °C differences with the temperature data. Reducing E_{max} will produce more segments, which decomposes the temperature profile into smaller pieces and allows detection of the thin epilimnion or hypolimnion, while increasing E_{max} will create a rougher representation, which may ignore important details in the profile. Fiedler (2010) used 3% of the temperature range from sea surface to sea bottom as E_{max}, which was too large for this data set and failed to detect thin epilimnion and hypolimnion. An extremely large E_{max} value will produce only one segment, which is just the linear regression of temperature values with depth.

The PLR algorithm generates L segments (Seg_1,Seg_2, ... ,Seg_L starting from lake surface to lake bottom), which are used to detect the epilimnion, TRM, and hypolimnion via the following criteria:

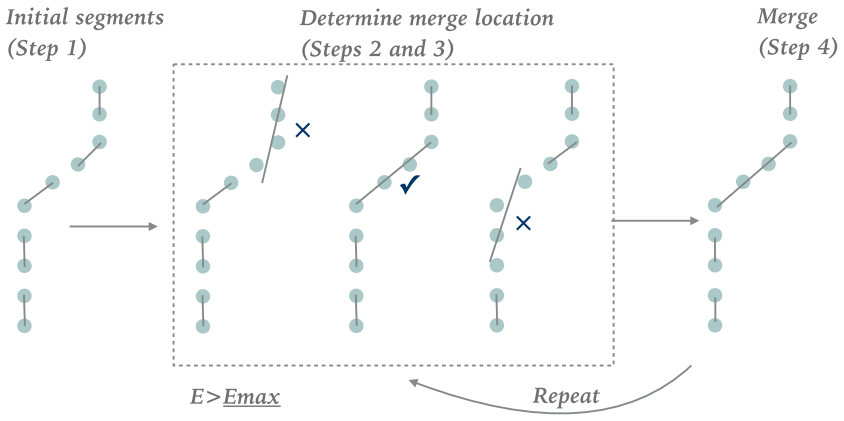

Figure 3. Algorithm workflow for piecewise linear representation.

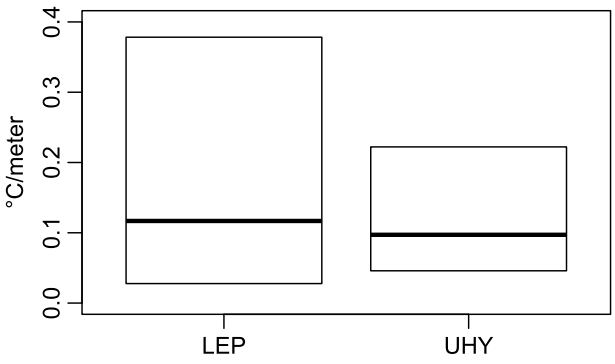

Figure 4. Boxplot of temperature gradients at depths of UHY (upper hypolimnion) and LEP (lower epilimnion) identified by operators in all lakes. The lower, middle, and upper lines in the box represent the first quantile, median, and third quantile values.

1. *TRM*. The depth of the middle point of the segment with maximum gradient is set as the TRM depth. To accommodate situations where no TRM appears in the profiles, we apply a threshold $g_{\min}^{\mathrm{TRM}}$ on the temperature gradient, below which the TRM does not exist in the profiles. Previous work gives different minimum gradients for the TRM, with values ranging from 0.05 °C/m (McCullough et al., 2007) to 1 °C/m (Watkins et al., 2015). We use a smaller threshold, 0.15 °C/m rather than 1 °C/m, because: (1) the segment approximation tends to smooth the raw gradient, so using 1 °C/m identifies fewer TRMs; and (2) in our data set, some profiles have mild temperature changes in the metalimnion due to already low surface temperatures.
2. *Epilimnion and hypolimnion*. Epilimnion and hypolimnion are stable water layers where the temperature gradient is small. We use the following approaches to identify epilimnion and hypolimnion:

   a. Scan surface segment to bottom and find index p so that Seg_i $(1 \le i \le p)$ has a temperature gradient less than a threshold $g(Seg_i) < g_{\mathrm{stable}}$ and total temperature from Seg_1 to Seg_p is less than $\Delta T_{\max} = 2^{\circ}\mathrm{C}$. Thus, the profile from Seg_1 to Seg_p is identified as the epilimnion.
   b. Examine from bottom segment to surface and find the index q so that for Seg_j $(q \le j \le L)$, $g(Seg_j) < g_{\mathrm{stable}}$ and total temperature from $Segq$ to $SegL$ is less than $\Delta T_{\max} = 2^{\circ}\mathrm{C}$. Then Seg_q to Seg_L is identified as the hypolimnion.

For our data sets, only including the topmost segment as the epilimnion (Thomson & Fine, 2003) generates epilimnion layers that are sometimes too thin to match the data well. In addition, it should be noted that in some cases the first (Seg_1) or last segments (Seg_L) sometimes have large gradients due to noise. To accommodate these edge cases, we relax the gradient threshold on the Seg_1 and Seg_L segments from g_{stable} to $g_{\mathrm{stable}}^{\mathrm{relax}}$, allowing the first and last segment to have larger gradients and to be included in the epilimnion and hypolimnion, respectively.

To determine g_{stable}, we first calculate temperature gradients at the depths of UHY and LEP from operators' notes, which are summarized in Figure 4. Since the operators have different judging criteria and depths may be mislabeled (discussed in section 3.1), the median values of the gradients (0.12 °C/m for lower epilimnion and 0.097 °C/m for UHY) are selected as reasonable estimates of stable water columns. Finally, we choose $g_{\mathrm{stable}} = 0.1^{\circ}\mathrm{C/m}$ and $g_{\mathrm{stable}}^{\mathrm{relax}} = 0.25^{\circ}\mathrm{C/m}$ by trial and error for this data set.

The differences between the above algorithm and the previous approach (Fiedler, 2010; Thomson & Fine, 2003) are as follows: (1) we use a bottom-up approach rather than the split and merge approach; (2) a smaller error $E_{\max}$ enables detection of thin epilimnion or hypolimnion in the profiles; and (3) we extend the model by using stable gradient constraints g_{stable} and temperature change constraints $\Delta T_{\max}$ to detect epilimnion and hypolimnion. We tested the split and merge approach on our case study and found similar performance to the bottom-up algorithm described above. However, the results depend on the splitting strategy, which adds more complexity. Furthermore, the split and merge algorithm did not converge in some edge cases when using maximum discrepancies as the error and using least squares to fit linear segments. The details on these differences are given in Appendix B.

2.3. DCL Detection Algorithm

We identify the DCL based on a peak detection algorithm that detects the number of peak points and their locations and then analyzes the shapes of each peak. Denote f_i and g_i as the fluorescence concentration and gradient at the ith point, starting from lake surface to the bottom, respectively. The gradient $g(i) = \frac{(f(i+1)-f(i))}{\Delta h}$), where Δh is the depth interval. The algorithm first finds all zero crossing points of g_i, which occur where the fluorescence gradient changes from positive to negative, meaning fluorescence concentration increases and then decreases. Then the algorithm filters out peaks that are not significant. The detailed steps are as follows (Figure 5):

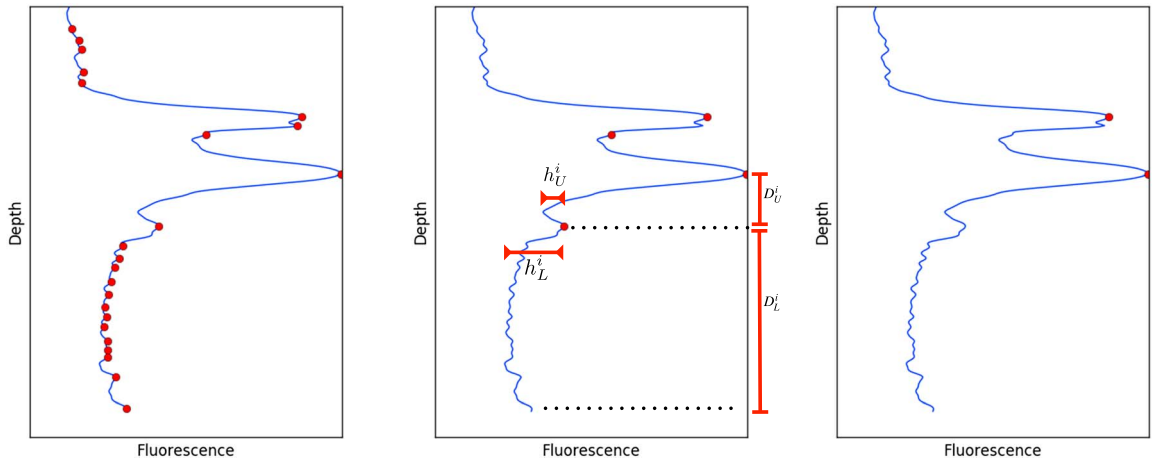

Step 1. Find all possible points

Steps 2 and 3. Remove the peaks with low magnitude and calculate the height of each peak

Steps 4 and 5. Remove the peaks that are not significant

Figure 5. Peak detection algorithm for identifying possible peaks and then filtering out insignificant peaks.

Step 1: Find the points where the gradient changes from positive to negative, that is, fluorescence concentration increases and then decreases. These zero crossing points are the potential peak points but may contain local maxima (e.g., see Figure 5, step 1). Denote $P^{(0)}$ as this set of peak candidate points.

Step 2: For each point in $P^{(0)}$, we apply a global threshold ($f_{\min}$) so that point P_i,$P_i \in P^{(0)}$ will be filtered out if $f_i < f_{\min}$. We also combine peaks that are close (within 2.5 m) by only considering the peak with the highest magnitude. Denote the remaining point set as $P^{(1)}$.

Step 3: For each point in $P^{(1)}$, denote D_U^i and D_L^i as the set of data within the upper and lower sides of the peak point i (e.g., see Figure 5). If i is the first peak from the lake surface, then D_U^i is the set of data from the first data point to the peak point. If point i is not the first peak point, then D_U^i is defined as the set of data from P_i to P_{i-1}. D_L^i follows a similar definition: D_L^i is the set of data from peak i to peak i+1 or to the last data point. Calculate $h_U^i = f_i - \min(D_U^i)$ and $h_L^i = f_i - \min(D_L^i)$. Then the height of peak i is $h_i = \min(h_U^i, h_L^i)$.

Step 4: Remove the peak point i from $P^{(1)}$ if $h_i < h_{\min}$. $h_{\min}$ is a threshold parameter set by trial and error that is related to how significant the peak should be.

Step 5: Repeat steps (3) and (4) until no points in $P^{(1)}$ can be removed. That is, all of the peaks left in $P^{(1)}$ are significant. If $P^{(1)}$ is empty, then there is no peak in the profile.

The peak boundaries (i.e., where the peak shape ends) are ill defined, especially for non-bell shape peaks or multiple peaks in the same profile. For profiles with only one peak, we fit two half Gaussian shapes with a linear trend of background concentration for the data above and below the peak, as follows:

$$\hat{y} = y_0 + k(x - x_0) + a \times \exp\left(\frac{-(x-x_0)^2}{2\sigma^2}\right) \quad (1)$$

where x is the depth, x_0 is the location of the peak point, and y_0+$k(x - x_0)$ is the background concentration with a trend k. We set $y_0 = \max(y) - a$ to align the magnitude of the Gaussian peak with the magnitude of the peak in the data, leaving only parameters k,a, and σ to be fit. To ensure that the increasing/decreasing stage is mostly captured by the Gaussian shape, we restrict k within a small range determined by trial and error as $[-0.15 \times K_{\text{thres}}, 0.15 \times K_{\text{thres}}]$, where K_{thres} is the gradient of the line connecting the peak point to the last point of the data to be fit.

The two half Gaussian shapes can have different parameter values so that nonsymmetric shapes can be fit. We define the DCL upper boundary as $\max(LEP, Depth_p - 2.5\sigma_1)$ and the lower boundary as $\min(\text{Max}(depth), Depth_p + 2.5\sigma_2)$, where LEP is the boundary between epilimnion and metalimnon, $Depth_p$ is the depth of the peak point, and σ_1,σ_2 are the standard deviations of the upper and lower Gaussian

Table 2
Stratification and DCL Detection Algorithm Parameters

Variable	Parameter	Definition	Value	Parameter effects
Therm-ocline	E_{max}	Maximum error in PLR approximation	0.30 °C	Smaller values will generate more and smaller segments, revealing more local structures
	g_{stable}	Maximum gradient of a stable water layer	0.10°/cm	Smaller values will determine a deeper hypolimnion. Too small values will generate no epilimnion or hypolimnion
	g_{stable}^{relax}	Maximum gradient of the first or last layer to be more robust in some profiles	0.25°/cm	Smaller values may result in no epilimnion or hypolimnion detected
	g_{min}^{TRM}	Minimum gradient for thermocline	0.15°/cm	Smaller values will tend to identify more profiles with mildly changing gradient
	ΔT_{max}	Total temperature change in epilimnion and hypolimnion	2 °C	Smaller values may lead to deeper hypolimnion or shallower epilimnion
Fluores-cence	f_{min}^{DCL}	Minimum magnitude of a peak	$\min(f)+0.3\times(\max(f)-\min(f))$	Smaller values will identify more peaks with low absolute peak magnitude
	h_{min}^{DCL}	Minimum height of a peak	$0.2\times(\max(f)-\min(f))$	Smaller values will identify more peaks with low relative peak magnitude (peak height)

shapes, respectively. The value of 2.5 is similar to the value recommended by Siswanto et al. (2005), who defined the half peak size as 2σ when fitting with only one ordinary Gaussian shape without the trend of the background concentration.

The final DCL depth is determined as the peak location with maximum fluorescence concentration and below the epilimnion, rather than the detected TRM. This is because the depth of the TRM may have different definitions among operators (discussed in the section 3.1). Therefore, setting the depth of the lower epilimnion as the DCL depth upper bound reduces the effects of TRM identification variations on DCL detection. As the moving average smoothing conducted in the data preprocessing stage may flatten the concentrations, the algorithm searches for the maximum fluorescence values C_m^{raw} in the raw data within 1 m around the detected DCL depth. C_m^{raw} is then selected as the final DCL concentration.

The parameters used in the lake stratification and DCL detection algorithms are summarized in Table 2.

2.4. Lake Heat Storage Computation

The detected lake stratification can also be used to compute heat absorbed into lakes between spring and summer, which reflects changes in evaporation, lake freezing, and water temperature (Derecki, 1976). For example, previous research has examined trends in lake surface temperatures in Lake Superior, which have been increasing since 1979, most likely due to declining winter ice cover and increases in air temperature and wind speed (Austin & Colman, 2007).

Changes in heat storage Q_t from time t_1 to t_2 can be computed as $Q_t = (V_2T_2 - V_1T_1)$ where V_i,T_i are the volume of the lake and average temperature at time t_i (Derecki, 1976). In this study, we calculated the heat storage change of a water column at each sampling site from spring to summer to assess heat absorbance during this period. The equation to calculate heat storage Q_i at each station from spring to summer is

$$Q_i = \int_{3\text{m}}^{h_i^{\text{UHY}}} \left(T_i^{\text{summer}}(h) - T_i^{\text{spring}}(h)\right) \mathrm{d}h \tag{2}$$

where h_i^{UHY} is the mean depth of the UHY at station i detected by the PLR algorithm (section 2.2). $T_i^{\text{summer}}(h), T_i^{\text{spring}}(h)$ are the temperatures at depth h in summer and spring at station i, respectively. In our case study, equation (2) is calculated from 3 m below the surface to the mean depth of UHY since the data in the top 3 m were removed due to data noise during preprocessing (section 2.1). Thus,Q_i computes the accumulated differences between the spring and summer temperature depth profiles above the mean UHY in the same year, which represents the cumulative effects of heating in the upper water column. Note that the spring profiles are computed using the same steps as the summer profiles, with a bin size of 0.25 m.

2.5. Algorithm Implementation and Web Applications

The detection algorithms are implemented using Python and its libraries Numpy, Scipy, Pandas, bekeh, and Flask. We also built an interactive Web application based on Flask web development framework (Figure 6

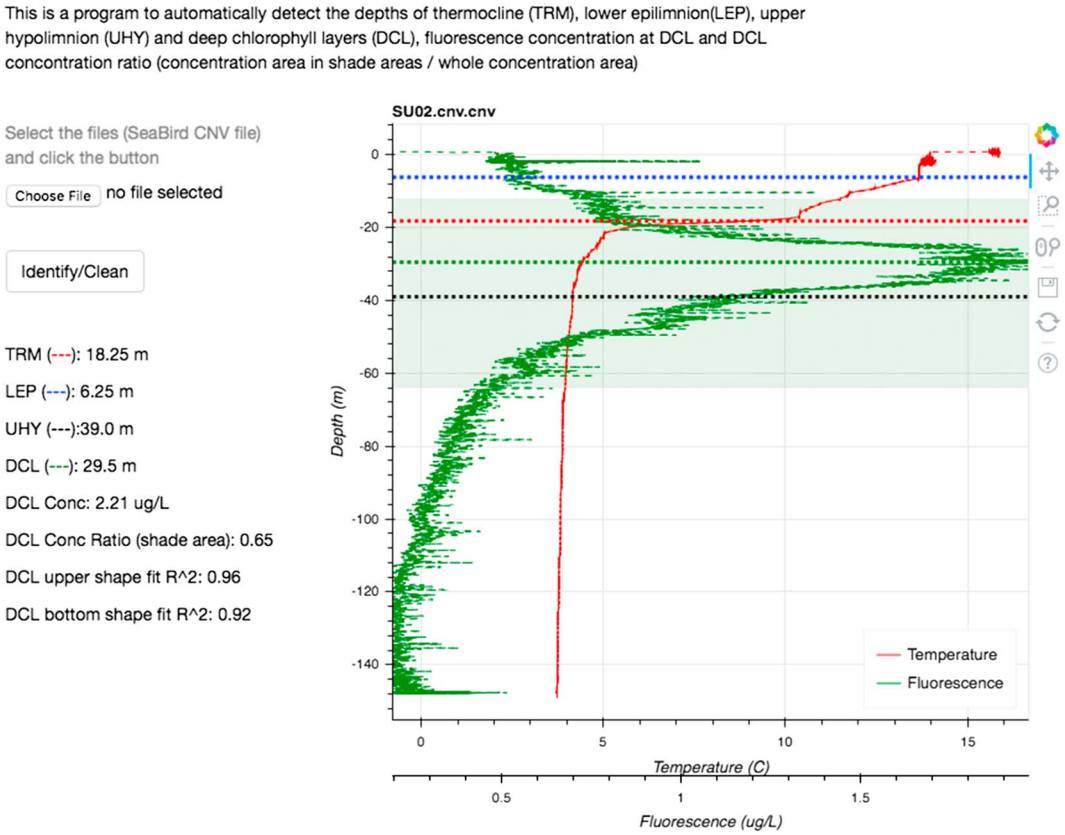

Figure 6. Web application interface. Thermoline (TRM), lower epilimnion (LEP), and upper hypolimnion (UHY) represents the depth of thermocline, lower epilimnion (the boundary between epilimnion and metalimnion), and upper hypolimnion (the boundary between metalimnion and hypolimnion).

contains a snapshot of the Web app). The Web application allows users to upload raw Sea-Bird CTD data files and computes the depths of TRM, LEP, UHY, and DCL, as well as DCL concentration with depth profiling plots. The code is open source (available at http://stormxuwz.github.io/SeabirdCode/).

3. Results

We applied the lake stratification and DCL detection algorithms on the Great Lakes profiles described previously. The results of the PLR lake stratification and peak detection algorithms are compared with historical operators' notes. Lake Superior is then used as a case study to reveal spatial and temporal trends of the TRM, DCL, and heat storage change from spring to summer. The mean depths of the UHY (h_i^{UHY}) for different stations in Lake Superior are summarized in Appendix C. We use ER, HU, MI, ON, and SU as the abbreviations for Lake Erie, Lake Huron, Lake Michigan, Lake Ontario, and Lake Superior, respectively.

3.1. Algorithm Validation

The PLR and peak detection algorithms are validated with existing operators' historical notes from 1998 to 2012, providing a total of 1,412 profiles. We first summarize in Figure 7 how many profiles in the data set have features detected by the algorithms only (green), by the operators only (yellow), by both (blue), or by neither (dark green).

The algorithms identify most of the features in operators' notes, with only limited profiles containing features that are only detected by operators (yellow portions in Figure 7). There are, however, many layers that are not captured in the operators' records (green portions in Figure 7). We use scatter plots to compare operator and algorithm-estimated depths (Figure 8) for each lake. Most algorithm estimates are comparable to recorded human judgments for TRM, LEP, and DCL detection. The discrepancies in UHY are generally large with small r^2 in Lakes Huron ($r^2 = 0.09$), Michigan ($r^2 = 0.20$), Ontario ($r^2 = 0.35$) and Superior ($r^2 = 0.20$),

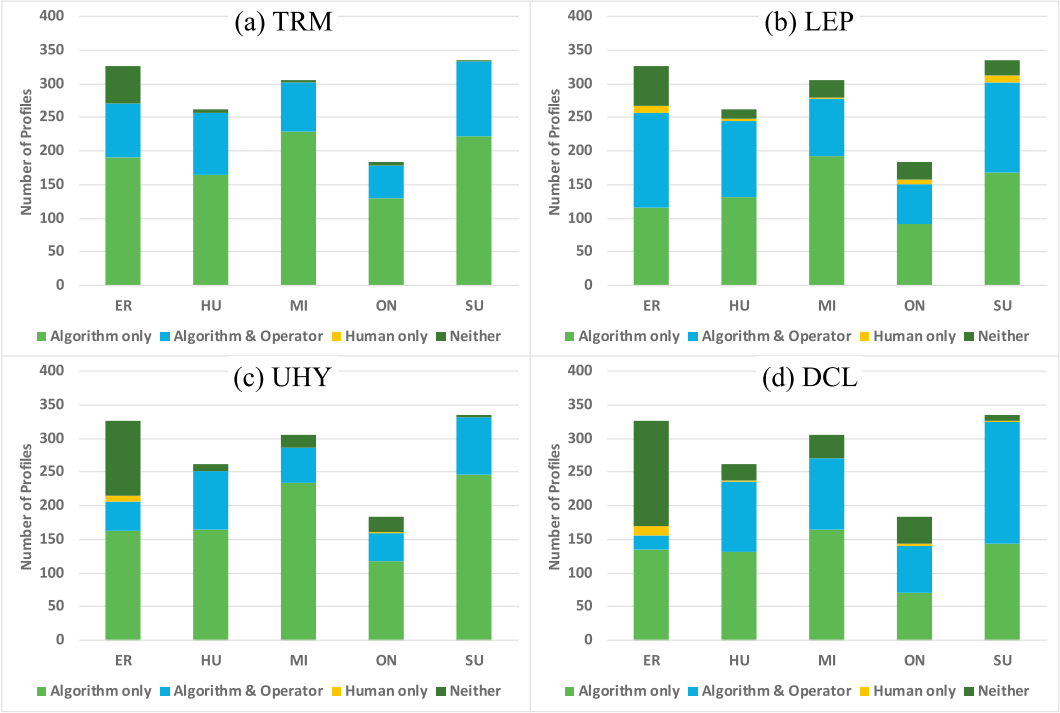

Figure 7. Number of profiles with features detected. (a) Thermocline (TRM), (b) lower epilimnion (LEP), (c) upper hypolimnion (UHY), and (d) deep chlorophyll layers (DCL).

but discrepancies are small in Lake Erie (r^2 = 0.77). It should be noted that r^2 and RMSE is heavily influenced by outliers and a low r^2 could be caused by a few outliers (Figure 8b, low r^2 in DCL detection).

By examining the profiles with larger discrepancies in more detail, we identify four categories that account for the differences, listed below. Figure 9 shows examples of these cases.

1. *Data mislabeled*. These outliers are due to operators' error or notes that are not corresponding to the correct profiles, which can occur when multiple casts are conducted by operators. For example, the DCL record of SU09 in 2011 is obviously incorrect in labeling the DCL as the peak point in the fluorescence profile (Figure 9a). This error was particularly prevalent in Lake Superior, where operators often labeled UHY using the depth of DCL, thus causing significant discrepancies (Figure 8e). Although some identifications may be reasonable (see *subjective ambiguity* discussion below), some operator labels are clearly incorrect.
2. *Algorithm limitations*. There are several algorithm parameters (Table 2) that are related to the sharpness of the TRM ($g_{\min}^{\mathrm{TRM}}$), the stability of the hypolimnion and epilimnion (g_{stable}), and the criteria to filter out shallow peaks ($f_{\min}^{\mathrm{DCL}}$ and $h_{\min}^{\mathrm{DCL}}$). For these parameters, we used the same values in all of the Great Lakes. However, these parameters may not always reflect the variability in operators' subjective judgment nor differing conditions in each lake. This type of errors accounts for most of the discrepancies in LEP detections, especially in Lake Erie, as some profiles in Lake Erie have larger temperature gradients in the epilimnion due to its shallowness. Therefore, the algorithm tends to detect a shallower LEP (Figure 8a). If no segments have gradients less than g_{stable}, the algorithms will fail to detect LEP (ER15 in 2009, Figure 9b) For DCL detection, some peaks are not detected, which could be caused by the moving average smoothing that can reduce the peak value. Another situation is that when no LEP is detected, the algorithm will then fail to detect DCL since DCL is the peak below LEP (section 2.3).
3. *Definition ambiguity*. The operator notes indicate that the operators may not always label TRM as the point where temperature changes most rapidly, nor DCL as the peak with the largest magnitude below the TRM. Many TRM discrepancies in Lakes Michigan, Ontario, and Huron (Figures 8b–8d where algorithms' depths are shallower) happen when the sharpest change is just below the LEP, but the operators define a deeper depth in the middle of the metalimnion as the TRM (e.g., Figure 9c). Fiedler (2010)

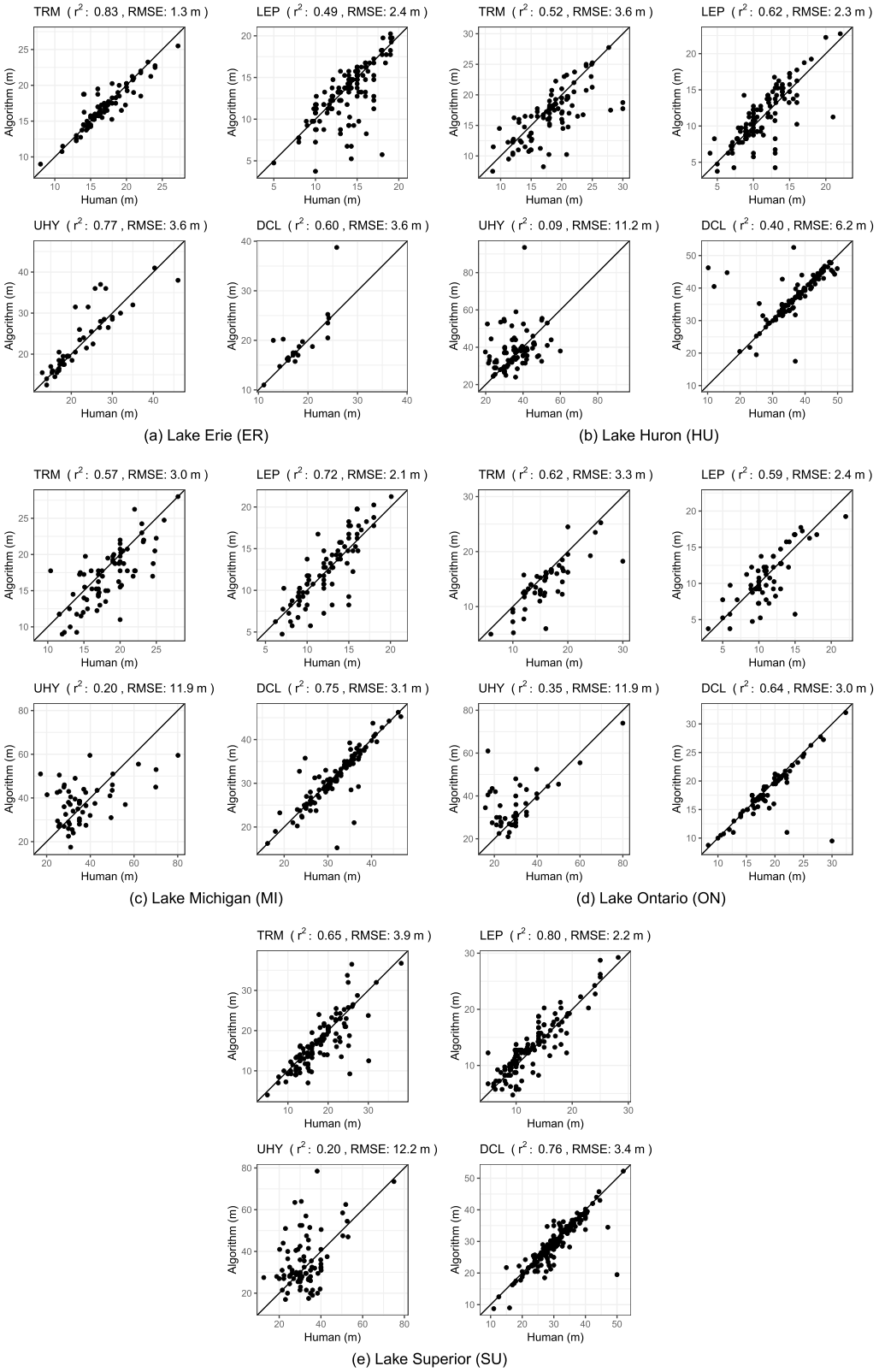

Figure 8. Comparisons between operators' and algorithm depth estimates for thermocline (TRM), lower epilimnion (LEP), upper hypolimnion (UHY), and deep chlorophyll layers (DCL) at (a) Lake Erie, (b) Lake Huron, (c) Lake Michigan, (d) Lake Ontario, and (e) Lake Superior.; "r^2" represents the squared correlation coefficients (or Coefficient of Determination) and "RMSE" represents the root-mean-square error.

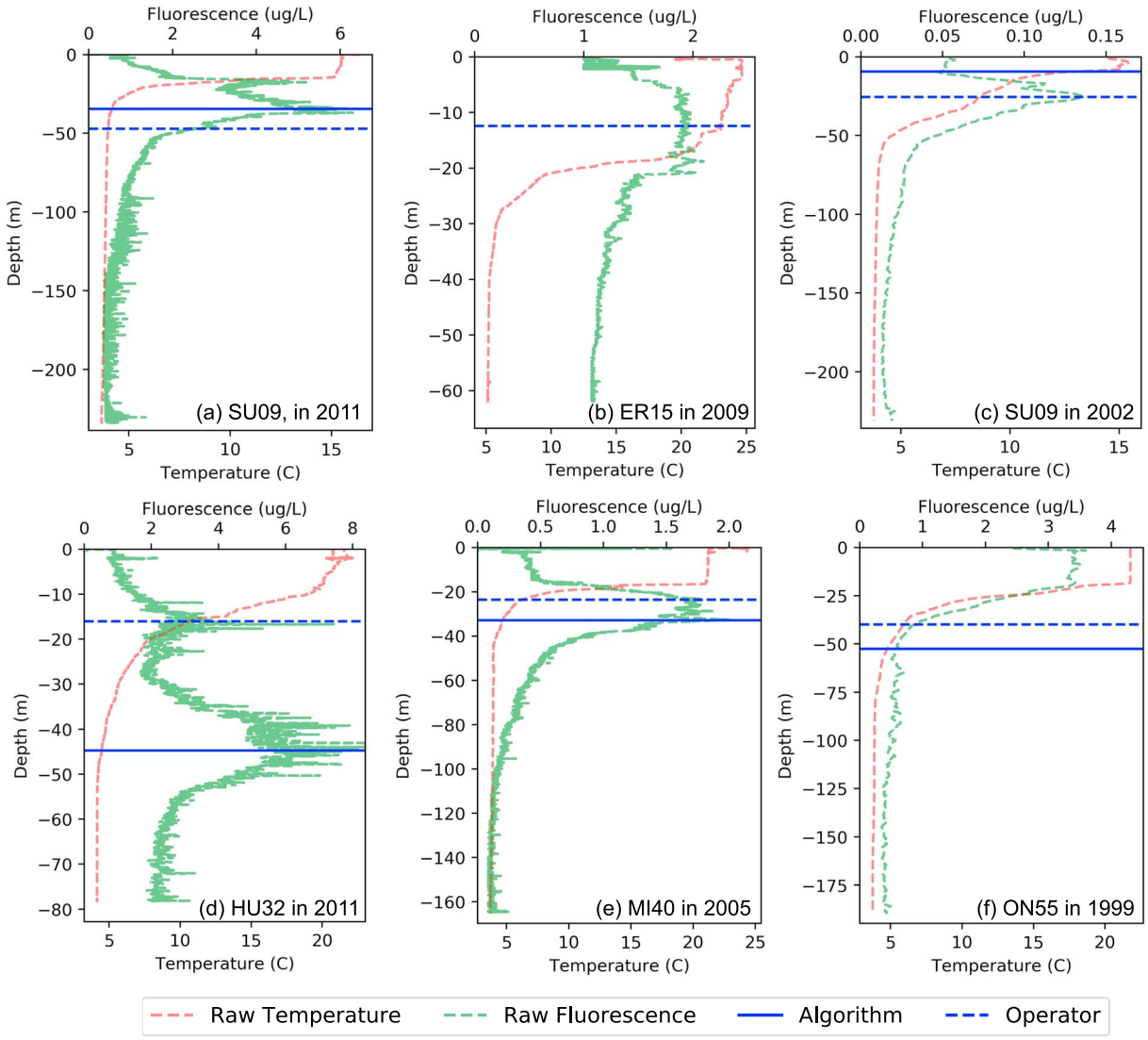

Figure 9. Outliers comparing algorithms and notes. (a) SU09 in 2011, DCL mislabeled; (b) ER15 in 2009, LEP failure; (c) SU09 in 2002, TRM definition; (d) HU32 in 2011, DCL definition; (e) MI40 in 2005, DCL subjectiveness; (f) ON55 in 1999, UHY subjectiveness. DCL = deep chlorophyll layers; LElower epilimnion; TRM = thermocline; UHY = upper hypolimnion.

suggests merging adjacent segments to the segment with maximum slope using another error tolerance parameter ($E'_{\max}$). However, this adjustment requires another parameter that must be tuned and still may not match the operator TRM, which is not always adjacent to the maximum gradient segment (e.g., Figure 9c).DCL definition ambiguity occurs when the first peak below the TRM is the DCL, while the algorithms select the second peak with the largest magnitude, although the algorithm can detect both peaks (e.g., HU32 in 2011, Figure 9d). Most of the large DCL differences in Lake Huron and Ontario are due to this double-peak structure in the profiles sampled during 2011. The double-peak structures indicate two locations for phytoplankton growth, and phytoplankton photoacclimation probably existed in the deeper peak due to light limitations.

4. *Subjective ambiguity*. In some cases, the fluorescence peak is very broad, and the exact largest point identified by the algorithms may differ from the notes (e.g., Station MI40 in Figure 9e). In addition, when the transition zone from metalimnion to hypolimnion is relatively smooth, the exact depth to separate the two layers is highly subjective (e.g., see Station ON55 from 1998 in Figure 9f). Such ambiguity accounts for the large UHY errors in Lakes Michigan, Ontario, and Huron. Lake Erie, on the other hand, usually has a sharp transition between metalimnion and hypolimnion, thus the algorithm performs well.

Overall, the algorithm mostly reflects the operators' criteria since majority of the detections are close to the operators' notes (dots near the 1:1 line in Figure 8) but cannot fully reflect the variability in highly subjective judgments made by individual operators. Moreover, it appears that some operators consider DCL depth as a close proxy to UHY since depths of operators' UHY and algorithms' DCL from some profiles are almost identical. Such UHY detection criteria are reasonable since DCL do often exist near the UHY.

3.2. Lake Superior Case Study

In this section, we apply the algorithms to profiles from Lake Superior and explore the spatiotemporal changes of lake features in the detection results.

3.2.1. Spatial and Temporal Trends of DCL and TRMs in Lake Superior

Without manually analyzing and identifying features, we execute the proposed algorithms and use glyph-maps (Wickham et al., 2012) to visualize the spatiotemporal trend of the features detected. In glyph-maps (Figure 10), boxes with trend graphs are located at the geographic sampling locations on the map. The upper and lower line represent the maximum and minimum values of all years and all stations (i.e., a global range). The horizontal line in the midrange is called the reference line, which is equal to the mean of the global maximum and minimum values. Glyph-maps help to understand the temporal trends as well as relative values across space. Note that for plots with depths (Figures 10a and 10b), higher points show data from shallower locations. A discontinuity (e.g., Station 23 in Figure 10a) indicates that no such features were detected in that year.

The TRM in Lake Superior ranges from 4 to 60 m. The thermostratifications in Lake Superior are heavily affected by wind, current, and corresponding upwelling (when warm surface water is pushed offshore by wind and cold bottom water rises toward the surface) and downwelling events (warm surface water is pushed toward the shore and sinks to the bottom). Specifically, the northwest shore (e.g., stations SU16, SU18, and SU19) had consistently shallow TRMs, which could be related to low temperatures caused by the eastward or southward currents and resulting north shore upwelling events (Bennett, 1978; Bennington et al., 2010). In the eastern basin, TRMs are generally deeper in the east south shore areas (e.g., SU21, SU05, and SU23), which may be due to a strong anticlockwise current (Bennington et al., 2010) and downwelling events caused by Ekman drift, in which surface water moves toward the prevailing wind directions in the Northern Hemisphere (Emery & Csanady, 1973).

Some stations have fluctuating TRM. For example, Station SU15 in 2009 (Figure 11a) and SU21 in 2010 (Figure 11b) have different profile shapes compared to other years, with deeper TRMs. Station SU21 is heavily influenced by the southward current to the east of Keweenaw Peninsula (Bennington et al., 2010), which can lead to downwelling events and a deepened TRM. The fluctuations could also be due to differences in total heat absorbed during that year, which is further discussed in section 3.2.2.

Most of the DCL depths from 1996 to 2013 are relatively stable (Figure 10b). However, Station SU23 has an increasing DCL depth in this period. For DCL concentrations (Figure 10c), almost all of the stations experienced two spikes in fluorescence concentrations (i.e., algae bloom) during this period. One spike occurred in 2000 and the other in 2011 (e.g., Figure 12a at SU07). White and Matsumoto (2012) used a three-dimensional numerical model to study the DCL in Lake Superior and showed that photoadaptation and the location of the nutricline (the depth where there is a rapid change in nutrients) are the primary factors determining DCL depths and concentrations, while zooplankton grazing and phytoplankton sinking secondarily affect DCL concentrations. Deeper nutriclines are also related to a longer stratification period (Barbiero & Tuchman, 2004). Therefore, the observed fluctuations in DCL depths (e.g., SU05 in Figure 12b) could be closely related to changes in light availability and lake stratifications. However, large internal wave motions could shift the DCL locations temporarily (Bouffard et al., 2018). Thus, the DCL depth fluctuations could also be caused by upwelling or downwelling events. The spikes in DCL concentrations during 2000 and 2011 could be related to more nutrient inputs, most likely phosphorus as Lake Superior is usually phosphorus deficient (Guildford et al., 2000).

3.2.2. Trend in Heat Storage From Spring to Summer in Lake Superior

Figure 13 summarizes the local trends in heat storage (Q_i) calculated from equation (2), at each sampling site in Lake Superior. A positive trend in Q_i means that the deep water is becoming increasingly heated from 1996 to 2013. Stations 03 ($p = 0.04$), 05 ($p = 0.10$), 07 ($p = 0.10$), 09 ($p = 0.03$), 10 ($p = 0.02$), 11 ($p = 0.04$),

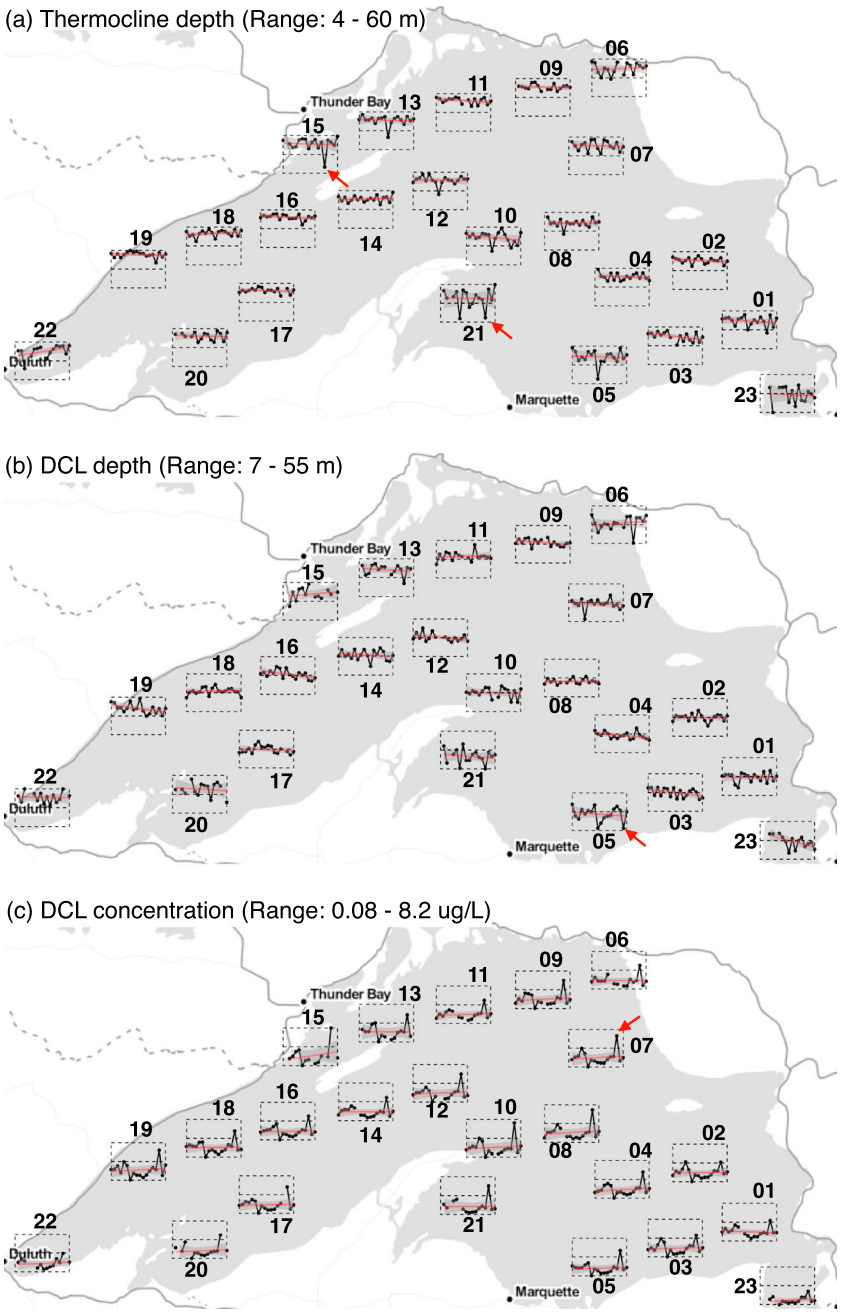

Figure 10. Glyph-maps of thermocline depth, DCL depth, and DCL concentrations from 1996 to 2013. The numbers are station indices. The red line is a linear trend. For plots with depths (a and b), a higher value indicates shallower depth. For plot (c), a higher value indicates high concentration. Red arrows are examples of exceptional data points illustrated in Figures 11 and 12. DCL = deep chlorophyll layers.

and 16 ($p = 0.04$) all have positive and significant linearly increasing trends from 1996 to 2013. In general, the stations in the eastern basin show a positive trend across the entire area. Since USEPA-GLNPO sampling dates are roughly the same every year and occur after the ice covering period, such a positive trend could be related to increased air temperature and wind speed and thus more heat absorbed by the lake (Austin & Colman, 2007). This is a phenomenon that appears to be happening across the Great Lakes (Collingsworth et al., 2017). Bathymetry also plays a role as the Great Lakes' summertime warming trend is positively related with lake depth (Zhong et al., 2018).

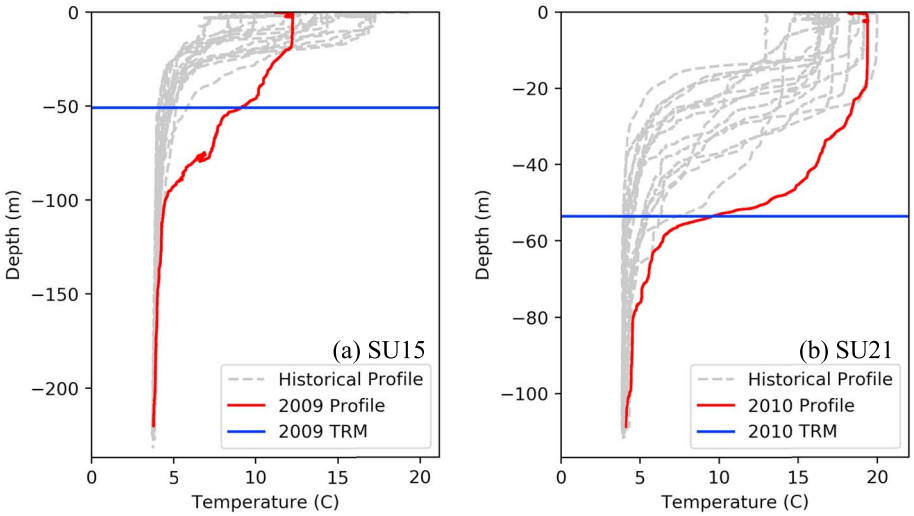

Figure 11. Temperature profile of Stations SU15 and SU21. Red lines represent thermocline profiles that are different from other years, shown by red arrows in Figure 10a. TRM = thermocline.

Note that Station 08 does not show a positive trend. Such an exception is probably due to a low average current speed since Station 08 is located near the center of the counterclockwise gyre (Bennington et al., 2010). Bennington et al. showed that external environmental changes (e.g., increased wind speed and air temperature) may have less effects on heat absorbance with low-speed currents.

In the western basin, a positive trend is not obvious at some sites, meaning that heat storage in the western basin from spring to summer is relatively consistent throughout the time series. Thus, the heating of the western basin described by Austin and Colman (2007) may be caused by declining winter ice cover, which leads to longer periods of solar radiation absorbance before the spring sampling. In addition, upwelling events that occurred in the northwest shoreline (Bennett, 1978; Bennington et al., 2010) may complicate lake stratification patterns and water column heating processes, thus resulting in the varying trends seen in Figure 13.

4. Discussion

Currently, historical profiles collected by USEPA-GLNPO are stored in databases, with some applications available to provide basic querying and visualization. The algorithms proposed here will provide more

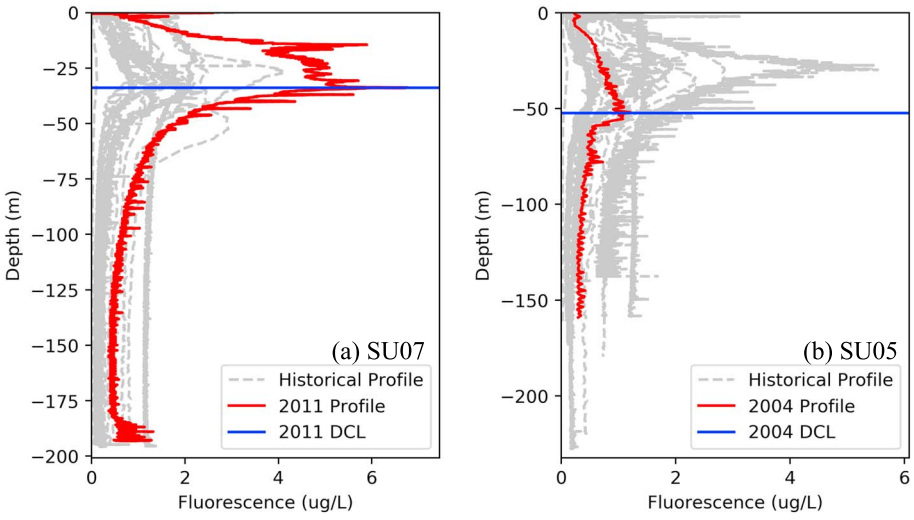

Figure 12. Fluorescence profile of Stations SU07 and SU05. Red lines are profiles that are different in a specific year compared to other years, shown by red arrows in Figures 10b and 10c. DCL = deep chlorophyll layers.

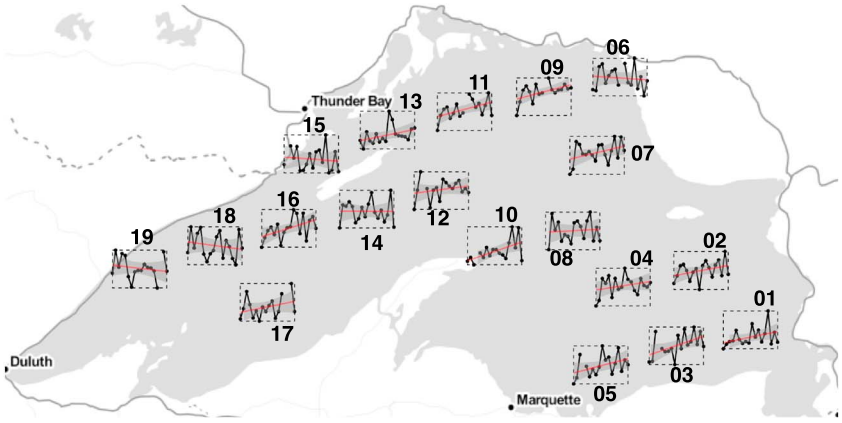

Figure 13. The local trend in heat storage changes from spring to summer at each site from 1996 to 2013. The values are scaled to [0,1] within each station. Red is the linear trend and the shaded area represents the 95% confidence interval. Discontinuities occur when no spring data were available that year.

advanced functions to more efficiently and consistently utilize the profile data. The algorithms characterize the whole profiles using a few parameters so that unusual shapes can easily be detected in the database or newly detected profiles. Besides querying basic features such as the depth of the TRM and DCL and the number of peaks, other advanced detection functions are proposed:

1. *Temperature profile anomalies such as sensor errors or double TRMs*. Sensor errors can be detected by highlighting segments with significant positive gradients. With double TRMs, the temperature drops rapidly, becomes stable, and then drops quickly again. Such phenomena may be caused by a residual TRM formed on a previous day (Ishikawa & Tanaka, 1993). We designed a simple double-search algorithm to find the Seg_i where the temperature gradients (g) of segment Seg_i, Seg_{i+1}, and Seg_{i-1} satisfy $g(Seg_{i+1}) > g_{\text{stable}}$, $g(Seg_i) < g_{\text{stable}}$, and $g(Seg_{i-1}) > g_{min}^{TRM}$, meaning Seg_{i+1} and Seg_{i-1} are not stable but Seg_i is
2. *DCL profile shapes*. We fit the DCL with two half-Gaussian shapes and define the normalized peak symmetry metric γ as

$$\gamma = \frac{\sigma_u - \sigma_l}{0.5(\sigma_u + \sigma_l)} \tag{3}$$

where σ_u,σ_l is the standard deviation of the half Gaussian shapes defined by equation (1) using the data above and below the DCL, respectively. The expression $\gamma > 0$ means that the peak has a milder gradient above the DCL than below the DCL. It should be noted that γ is dependent on the standard deviation of the Gaussian shapes. When Gaussian shapes characterize the data poorly, then γ is not a good representation of the DCL shape.

The DCLs in Lake Ontario generally have sharper gradients in fluorescence concentrations above the DCL, with $\gamma < 0$. One possible explanation for the asymmetric DCL shape (Figure 14) could be due to predator grazing such as zooplankton and fish (Benoit-Bird et al., 2009). Fluorescence gradient above the DCL will be steeper when more zooplankton are presented, which can further be related to fish distribution (Benoit-Bird et al., 2009; Durham & Stocker, 2012). Symmetric shapes (e.g., Figure 13b) occur when zooplankton are in low abundance (Benoit-Bird et al., 2009). In addition, the steepness (σ_u,σ_l in equation (3)) could be related to turbulent mixing, direct swimming to the DCL, and vertical shear (Birch et al., 2009).

In addition, the features derived from the algorithms contribute to cluster analyses that group similar profiles, confirming previous research (Richardson et al., 2002). By analyzing the clusters across space and time, the seasonal and location variability of the depth profiles can be revealed.

Overall, this type of characterization of depth profiling data benefits future sampling activities by (1) providing a consistent method for detection of lake stratification patterns and DCL, as well as comparisons with historical notes to highlight unusual patterns and correct notes if needed; (2) detecting additional features such as symmetry of DCL shapes and comparison of shapes from current and historical profiles, which

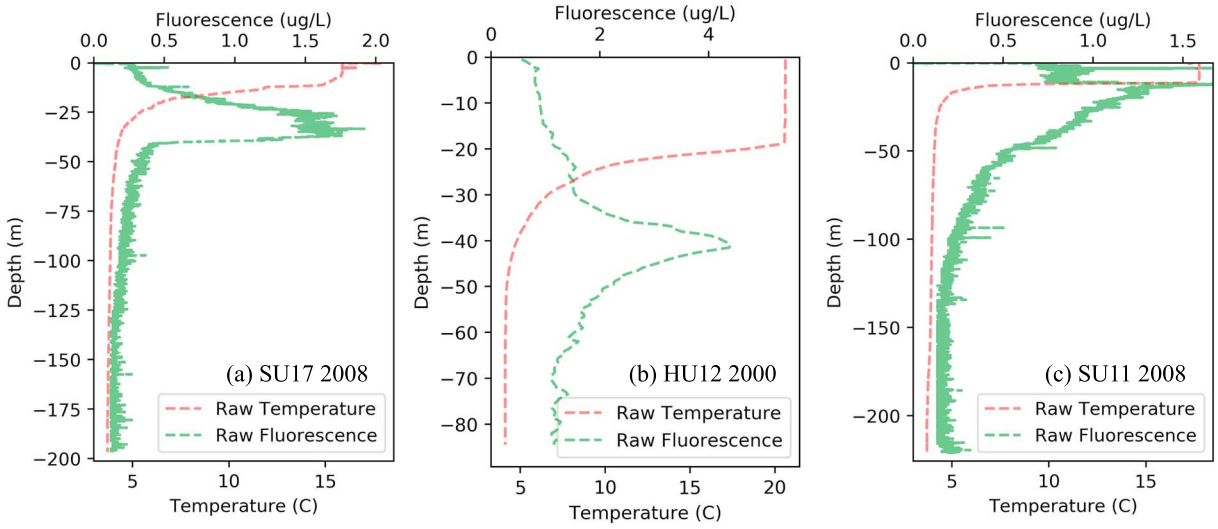

Figure 14. The shapes of DCLs with different symmetric patterns. (a) Peak has mild increasing but sharp decreasing gradient ($\gamma = 1.46$); (b) Peak has relatively consistent increasing and decreasing gradient ($\gamma = 0.003$); (c) Peak has sharp increasing but mild decreasing gradient ($\gamma = -1.84$).

could benefit adaptive sampling activities to immediately collect more data on unusual profiles; and (3) the Web application facilitates operators and researchers without programming knowledge to easily use the algorithms.

It should be emphasized that the algorithms are not intended to replace human judgment, but rather to provide rapid information for applying judgment where needed, such as making assessments during sampling activities and extracting general patterns from a large database. For example, for (1) above, data belonging to the same station can be plotted in a boxplot of absolute depth differences between algorithm and operators' results. The outliers in the boxplot would then indicate large deviations that need further checking. If no human labels are available, the temporal trend of a certain feature can be plotted using glyph plots (e.g., Figures 10 and 13) or a boxplot summary of features in all years at one station. The outliers in these plots will indicate unusual profiles for operators to check further. This could significantly reduce labor without sacrificing quality.

5. Conclusions

We extend PLR algorithms and propose a peak detection algorithm to automatically identify stratification and DCL patterns, providing a consistent method to identify lake features. The algorithms generally produced similar results to human judgment, with squared correlation coefficients around 0.6 for LEP, TRM, and DCL detection. Differences between human judgment and the algorithm results revealed many inconsistencies in the operators' judging criteria, such as using DCL as UHY and identifying TRM at a different depth from the sharpest gradient. The algorithms also highlighted anomalous patterns such as double TRMs and unusual peak shapes. A visualization of the general patterns of lake stratification and DCL in Lake Superior shows how the algorithms can provide insights on spatiotemporal changes in lake processes.

We caution that a careful model parameter tuning process is needed when the algorithms are extended to other lake systems (Fiedler, 2010). If depth labels (i.e., the locations of TRM, LEP, and UHY) are available as in this study, users can calculate the gradients of the labeled data (i.e., temperature gradients of the TRM as well as gradients of the epilimnion and hypolimnion), and these gradients derived from labeled data can then be used as a starting point to determine the parameters of the detection model (Figure 4). The temperature gradient of the TRM can be used to determine the minimum TRM gradient threshold ($g_{\text{min}}^{\text{TRM}}$ in Table 2) and the gradients of the epilimnion and hypolimnion can be used as the initial guess of the gradient of stable water layers (g_{stable} in Table 2).

We experimented with several parameter values to identify which correctly reveal patterns of typical profiles (profiles with obvious three-layer stratifications). Then we examined profiles with identified depths that

were very different from the human operator labels. If LEP is too shallow (or UHY is too deep) with too many segments, we either increased E_{max} to generate fewer segments or increased the gradient threshold (g_{stable}) to include more segments in the epilimnion (or hypolimnion). For DCL detection parameters, we checked several profiles with different parameters to see whether those peaks are visually correct (e.g., correct peak location and reasonable peak boundaries). The parameters related to DCL detections (f_{min}^{DCL} and h_{min}^{DCL}) depend on the maximum and minimum concentrations in a profile, which provides some capability to adjust based on different profiles. For other data sets with no operator labels, we suggest trying different parameters for some typical profiles first and manually examining the results. Then fine tune the parameters to consider more diverse profiles. Once the parameters are satisfactory, this set of parameters can be used for all other profiles.

The algorithms describe two typical ways to characterize the depth profiling data that can be extended to other water quality data in the lakes. Conductivity and other nutrient data can be similarly analyzed with temperature profiles to detect the halocline and chemocline where a sharp salinity or chemical gradient exists (Boehrer & Schultze, 2008). The peak of dissolved oxygen can be automatically detected by the peak detection algorithm and compared with the DCL data, allowing limnologists to study patterns in the locations of DCL and dissolved oxygen peaks. For example, Scofield et al. (2017) found cooccurrences of DCL with dissolved oxygen peaks in Lake Ontario. The algorithms could also be easily adapted to detect features in data sampled from undulating vehicles. This would allow changes in TRM or DCL along the ships' path to be revealed.

Appendix A

The temperature and chlorophyll concentration are measured by SBE 3plus 6,800-m depth rated Temperature Sensor and Seapoint Fluorometer (SCF-3549 Fluorometer), respectively. Additional instruments on SeaBird include SBE Conductivity 4C 6,800-m depth rated Conductivity Sensor, SBE 43 6,800-m depth rated Dissolved Oxygen Sensor, SBE 32 Carousel Water Sampler, Surface PAR Sensor model QSR 2200, Underwater PAR sensor model QSP-2300, C-STAR transmissometer, Suna Nitrate Sensor, Teledyne Benthos Altimeter (PSA-916 Sonar Altimeter), Rosette Standard ES (Model 115 Niskin Bottle), and SBE 11+ Deck Unit. All instruments are connected to 9plus CTD.

Appendix B

The split and merge algorithm proposed by Thomson and Fine (2003) has many similarities with our algorithms. Denote the $E(Seg_i)$ as the approximation error of Segment i. The approximation error is defined as the maximum discrepancies of the linear segment approximation and the raw series, that is, $E = \max(abs(y-\hat{y}))$ where y and $\hat{y}$ are the data and fitted values, as in our algorithm. The basic steps in the split and merge algorithm are as follows:

Step 1: Given initial segments, split Seg_s into Seg_{s1} and Seg_{s2} if the approximation error $E(Seg_s)$ is larger than a threshold E_{max};
Step 2: Merge Seg_k and Seg_{k+1} if the E of merged segment is less than E_{max};
Step 3: For adjacent segments Seg_k and Seg_{k+1}, scan the break position to reduce $\max(E(Seg_k), E(Seg_{k+1}))$;

Repeat Step 1 to Step 3 until no segments are changed.

Through experimentation, we found that the results of the split and merge algorithm depend on how splitting is done. Different split strategies (selection of the splitting point) will generate segments with slightly different gradients, which can lead to the following:

a. Different TRM because the segment with maximum gradient is changed.
b. Different LEP and UHY because the segments that satisfy stable water constraints (section 2.2) are changed.

In addition, after experimenting with different splitting strategies, we found that the algorithm does not converge for some profiles under some splitting strategies. The detailed reasons are described below.

In our study, the error function is the maximum discrepancy. After splitting Seg_s, into Seg_{s1} and Seg_{s2},it is possible that one of the new segments has a larger approximation error E than the original segment, for example, $E(Seg_{s2}) > E(Seg_s)$. This is because linear segments are fitted by the least squares method to reduce $\sum(y-\hat{y})^2$ rather than reduce $\max(abs(y-\hat{y}))$.

Next, suppose Seg_{s1} is merged with a previous segment Seg_k to form Seg_{k+s1}. In the breaking point adjustment step (Step 3), the boundaries between Seg_{k+s1} and Seg_{s2} must be adjusted to minimize $\max(E(Seg_{k+s1}), E(Seg_{s2}))$. Since $E(Seg_{s1+s2}) < E(Seg_{s2})$, the algorithm may again adjust as Seg_k and Seg_{s1+s2}. As a result, we are back to the starting point with Seg_s, and the algorithm will not converge.

Appendix C

Table C1 provides mean depths of UHY in Lake Superior.

Table C1
Mean Depth of UHY (h_i^{UHY}) at Each Station

Station	Mean UHY depth (m)	Station	Mean UHY depth (m)
SU01	36.86	SU11	27.24
SU02	28.19	SU12	30.58
SU03	33.94	SU13	30.61
SU04	28.18	SU14	29.69
SU05	39.25	SU15	41.65
SU06	46.29	SU16	30.28
SU07	31.79	SU17	30.21
SU08	35.56	SU18	25.03
SU09	33.09	SU19	23.64
SU10	46.67		

Acknowledgments
This manuscript is publication IISG19-HCE-SCI-040 of Illinois-Indiana Sea Grant. All data are maintained by EPA. They are publicly available and can be accessed by contacting Jeff May (may.jeffery@epa.gov). We also provide algorithm code, plotting code, all calculated features, and sample data in the supporting information. They are also publicly available at http://stormxuwz.github.io/SeabirdCode/

References

Abbott, M. R., Denman, K. L., Powell, T. M., Richerson, P. J., Richards, R. C., & Goldman, C. R. (1984). Mixing and the dynamics of the deep chlorophyll maximum in Lake Tahoe1. *Limnology and Oceanography*, *29*(4), 862–878.

Austin, J. A., & Colman, S. M. (2007). Lake Superior summer water temperatures are increasing more rapidly than regional air temperatures: A positive ice-albedo feedback. *Geophysical Research Letters*, *34*, L06604. https://doi.org/10.1029/2006GL029021

Barbiero, R. P., & Tuchman, M. L. (2004). The deep chlorophyll maximum in Lake Superior. *Journal of Great Lakes Research*, *30*, 256–268.

Beckmann, A., Hense, I., 2007. Beneath the surface: Characteristics of oceanic ecosystems under weak mixing conditions—A theoretical investigation. *Progress in Oceanography 75* (4), 771–796.

Bennett, E. B. (1978). Characteristics of the thermal regime of Lake Superior. *Journal of Great Lakes Research*, *4*(3), 310–319.

Bennington, V., McKinley, G. A., Kimura, N., & Wu, C. H. (2010). General circulation of Lake Superior: Mean, variability, and trends from 1979 to 2006. *Journal of Geophysical Research*, *115*, C12015. https://doi.org/10.1029/2010JC006261

Benoit-Bird, K. J., Cowles, T. J., & Wingard, C. E. (2009). Edge gradients provide evidence of ecological interactions in planktonic thin layers. *Limnology and Oceanography*, *54*(4), 1382–1392.

Birch, D. A., Young, W. R., & Franks, P. J. S. (2009). Plankton layer profiles as determined by shearing, sinking, and swimming. *Limnology and Oceanography*, *54*(1), 397–399.

Boehrer, B., & Schultze, M. (2008). Stratification of lakes. *Reviews of Geophysics*, *46*, RG2005. https://doi.org/10.1029/2006RG000210

Bouffard, D., Ackerman, J. D., & Boegman, L. (2013). Factors affecting the development and dynamics of hypoxia in a large shallow stratified lake: Hourly to seasonal patterns. *Water Resources Research*, *49*, 2380–2394. https://doi.org/10.1002/wrcr.20241

Bouffard, D., Kiefer, I., Wüest, A., Wunderle, S., & Odermatt, D. (2018). Are surface temperature and chlorophyll in a large deep lake related? An analysis based on satellite observations in synergy with hydrodynamic modelling and in-situ data. *Remote Sensing of Environment*, *209*, 510–523.

Bramburger, A. J., & Reavie, E. D. (2016). A comparison of phytoplankton communities of the deep chlorophyll layers and epilimnia of the Laurentian Great Lakes. *Journal of Great Lakes Research*, *42*(5), 1016–1025.

Camacho, A. (2006). On the occurrence and ecological features of deep chlorophyll maxima (DCM) in Spanish stratified lakes. *Limnetica*, *25*, 453–478.

Collingsworth, P. D., Bunnell, D. B., Murray, M., Yu-Chun, K., Claramunt, R., Feiner, Z. S., et al. (2017). Climate change as a long-term stressor for the fisheries of the Laurentian Great Lakes of North America. *Reviews in Fish Biology and Fisheries*, *27*, 363–391.

Cullen, J. J. (2015). Subsurface chlorophyll maximum layers: Enduring enigma or mystery solved? *Annual Review of Marine Science*, *7*(1), 207–239.

Derecki, J. A. (1976). Heat storage and advection in Lake Erie. *Water Resources Research*, *12*(6), 1144–1150. https://doi.org/10.1029/WR012i006p01144

Durham, W. M., & Stocker, R. (2012). Thin phytoplankton layers: Characteristics, mechanisms, and consequences. *Annual Review of Marine Science*, *4*, 177–207.
Emery, K. O., & Csanady, G. T. (1973). Surface circulation of lakes and nearly land-locked seas. *Proceedings of the National Academy of Sciences of the United States of America*, *70*(1), 93–97.
Fahnenstiel, G. L., & Scavia, D. (1987). Dynamics of Lake Michigan phytoplankton: The deep chlorophyll layer. *Journal of Great Lakes Research*, *13*(3), 285–295.
Fiedler, P. C. (2010). Comparison of objective descriptions of the thermocline. *Limnology and Oceanography: Methods*, *8*(6), 313–325.
Gong, X., Shi, J., Gao, H. W., & Yao, X. H. (2015). Steady-state solutions for subsurface chlorophyll maximum in stratified water columns with a bell-shaped vertical profile of chlorophyll. *Biogeosciences*, *12*(4), 905–919.
Gorham, E., & Boyce, F. M. (1989). Influence of lake surface area and depth upon thermal stratification and the depth of the summer thermocline. *Journal of Great Lakes Research*, *15*(2), 233–245.
Guildford, S. J., Bootsma, H. A., Fee, E. J., Hecky, R. E., & Patterson, G. (2000). Phytoplankton nutrient status and mean water column irradiance in Lakes Malawi and Superior. *Aquatic Ecosystem Health & Management*, *3*(1), 35–45.
Hampton, S. E., Gray, D. K., Izmest'eva, L. R., Moore, M. V., & Ozersky, T. (2014). The rise and fall of plankton: Long-term changes in the vertical distribution of algae and grazers in Lake Baikal, Siberia. *PLoS ONE*, *9*(2), e88920.
Ishikawa, T., & Tanaka, M. (1993). Diurnal stratification and its effects on wind-induced currents and water qualities in Lake Kasumigaura, Japan. *Journal of Hydraulic Research*, *31*(3), 307–322.
Keogh, E., Chu, S., Hart, D., & Pazzani, M. (2004). Segmenting time series: A survey and novel approach. In *Data Mining in Time Series Databases*, *Series in Machine Perception and Artificial Intelligence* (Vol. 57, pp. 1–21). World Scientific. https://doi.org/10.1142/9789812565402_0001
Klausmeier, C. A., & Litchman, E. (2001). Algal games: The vertical distribution of phytoplankton in poorly mixed water columns. *Limnology and Oceanography*, *46*(8), 1998–2007.
Lips, U., & Lips, I. (2014). Bimodal distribution patterns of motile phytoplankton in relation to physical processes and stratification (Gulf of Finland, Baltic Sea). *Deep-Sea Research Part 2: Topical Studies in Oceanography*, *101*, 107–119.
Lorenzen, C. J. (1966). A method for the continuous measurement of in vivo chlorophyll concentration. *Deep Sea Research and Oceanographic Abstracts*, *13*(2), 223–227.
McCullough, G. K., Barber, D., & Cooley, P. M. (2007). The vertical distribution of runoff and its suspended load in Lake Malawi. *Journal of Great Lakes Research*, *33*(2), 449–465.
Mellard, J. P., Yoshiyama, K., Litchman, E., & Klausmeier, C. A. (2011). The vertical distribution of phytoplankton in stratified water columns. *Journal of Theoretical Biology*, *269*(1), 16–30.
Moukomla, S., & Blanken, P. D. (2016). Remote sensing of the North American Laurentian Great Lakes surface temperature. *Remote Sensing*, *8*(4), 286.
Oliver, S. K., Branstrator, D. K., Hrabik, T. R., Guildford, S. J., & Hecky, R. E. (2014). Nutrient excretion by crustacean zooplankton in the deep chlorophyll layer of Lake Superior. *Canadian Journal of Fisheries and Aquatic Sciences*, *72*(3), 390–399.
Oppenheim, A. V., Schafer, R. W., & Buck, J. R. (1999). *Discrete-Time Signal Processing*, (p. 468). Upper Saddle River: Prentice-Hall.
Pavlidis, T., & Horowitz, S. L. (1974). Segmentation of plane curves. *IEEE Transactions on Computers*, *C-23*(8), 860–870.
Richardson, A. J., Pfaff, M. C., Field, J. G., Silulwane, N. F., & Shillington, F. A. (2002). Identifying characteristic chlorophyll-a profiles in the coastal domain using an artificial neural network. *Journal of Plankton Research*, *24*(12), 1289–1303.
Ryabov, A. B., Rudolf, L., & Blasius, B. (2010). Vertical distribution and composition of phytoplankton under the influence of an upper mixed layer. *Journal of Theoretical Biology*, *263*(1), 120–133.
Scofield, A. E., Watkins, J. M., Weidel, B. C., Luckey, F. J., & Rudstam, L. G. (2017). The deep chlorophyll layer in Lake Ontario: Extent, mechanisms of formation, and abiotic predictors. *Journal of Great Lakes Research*, *43*(5), 782–794.
Siswanto, E., Ishizaka, J., & Yokouchi, K. (2005). Estimating chlorophyll-a vertical profiles from satellite data and the implication for primary production in the Kuroshio front of the East China Sea. *Journal of Oceanography*, *61*, 575–589.
Thomson, R. E., & Fine, I. V. (2003). Estimating mixed layer depth from oceanic profile data. *Journal of Atmospheric and Oceanic Technology*, *20*(2), 319–329.
Uitz, J., Claustre, H., Morel, A., & Hooker, S. B. (2006). Vertical distribution of phytoplankton communities in open ocean: An assessment based on surface chlorophyll. *Journal of Geophysical Research*, *111*, C08005. https://doi.org/10.1029/2005JC003207
Wang, B., Wu, R., & Lukas, R. (2000). Annual adjustment of the thermocline in the tropical Pacific Ocean. *Journal of Climate*, *13*(3), 596–616.
Watkins, J. M., Weidel, B. C., Rudstam, L. G., & Holeck, K. T. (2015). Spatial extent and dissipation of the deep chlorophyll layer in Lake Ontario during the Lake Ontario lower foodweb assessment, 2003 and 2008. *Aquatic Ecosystem Health and Management*, *18*(1), 18–27.
White, B., & Matsumoto, K. (2012). Causal mechanisms of the deep chlorophyll maximum in Lake Superior: A numerical modeling investigation. *Journal of Great Lakes Research*, *38*(3), 504–513.
Wickham, H., Hofmann, H., Wickham, C., & Cook, D. (2012). Glyph-maps for visually exploring temporal patterns in climate data and models. *Environmetrics*, *23*(5), 382–393.
Yu, H., Tsuno, H., Hidaka, T., & Jiao, C. (2010). Chemical and thermal stratification in lakes. *Limnology*, *11*(3), 251–257.
Zhong, Y., Notaro, M., & Vavrus, S. J. (2018). Spatially variable warming of the Laurentian Great Lakes: an interaction of bathymetry and climate. *Climate Dynamics*.